



Interpretation of runaway electron synchrotron and bremsstrahlung images

Downloaded from: <https://research.chalmers.se>, 2024-03-13 09:17 UTC

Citation for the original published paper (version of record):

Hoppe, M., Embréus, O., Paz-Soldan, C. et al (2018). Interpretation of runaway electron synchrotron and bremsstrahlung images. Nuclear Fusion, 58(8). <http://dx.doi.org/10.1088/1741-4326/aaae15>

N.B. When citing this work, cite the original published paper.

Interpretation of runaway electron synchrotron and bremsstrahlung images

M. Hoppe¹, O. Embréus¹, C. Paz-Soldan², R.A. Moyer³ and T. Fülöp¹

¹ Department of Physics, Chalmers University of Technology, Göteborg, Sweden

² General Atomics, San Diego, CA 92186, United States of America

³ University of California—San Diego, La Jolla, CA 92093, United States of America

E-mail: hoppe@chalmers.se

Received 6 December 2017, revised 25 January 2018

Accepted for publication 9 February 2018

Published 22 June 2018



Abstract

The crescent spot shape observed in DIII-D runaway electron synchrotron radiation images is shown to result from the high degree of anisotropy in the emitted radiation, the finite spectral range of the camera and the distribution of runaways. The finite spectral camera range is found to be particularly important, as the radiation from the high-field side can be stronger by a factor 10^6 than the radiation from the low-field side in DIII-D. By combining a kinetic model of the runaway dynamics with a synthetic synchrotron diagnostic we see that physical processes not described by the kinetic model (such as radial transport) are likely to be limiting the energy of the runaways. We show that a population of runaways with lower dominant energies and larger pitch-angles than those predicted by the kinetic model provide a better match to the synchrotron measurements. Using a new synthetic bremsstrahlung diagnostic we also simulate the view of the gamma ray imager diagnostic used at DIII-D to resolve the spatial distribution of runaway-generated bremsstrahlung.

Keywords: runaway electron, synchrotron radiation, bremsstrahlung, synchrotron image, tokamaks, synthetic diagnostic

(Some figures may appear in colour only in the online journal)

1. Introduction

In the presence of a sufficiently strong electric field, thermal electrons can be accelerated to relativistic energies, and are commonly referred to as runaway electrons [1]. In tokamak disruptions, when the plasma current changes quickly and a strong electric field is induced, these electrons can carry a large fraction of the plasma current. If control of the plasma is then lost, the runaway electron beam will collide with the walls and can inflict severe damage. Therefore, the runaway electron phenomenon is regarded as among the greatest threats to future fusion reactors [2–6] and the performance of ITER relies on the successful mitigation of these relativistic particles.

Due to their highly relativistic motion, runaway electrons will emit radiation [7, 8] almost entirely along their velocity vectors. The strong anisotropy of the radiation means that it contains information not only about the energy and radial distributions, but also about the pitch-angle distribution. Since it is emitted mainly at infra-red, and sometimes even visible wavelengths, synchrotron radiation is therefore an accessible diagnostic allowing indirect measurements of the runaway electron distribution function. The wealth of information contained in the synchrotron radiation also makes it an attractive candidate for benchmarking models of runaway dynamics.

Synchrotron radiation from runaway electrons was first studied on the TEXTOR tokamak [9] and has since been applied to many other tokamaks to study the runaway electron distribution function [10–23]. Basic interpretation of the synchrotron radiation data obtained in experiments has been done ever since the first synchrotron radiation measurements, but in 1996 the first deeper analysis of the synchrotron radiation spot shape seen in camera images was carried out by Pankratov



Original content from this work may be used under the terms of the [Creative Commons Attribution 3.0 licence](https://creativecommons.org/licenses/by/3.0/). Any further distribution of this work must maintain attribution to the author(s) and the title of the work, journal citation and DOI.

[24], and later in 1999 the effects of the toroidal geometry on the synchrotron radiation spectrum were also considered [25]. The next major step in the modeling of synchrotron radiation came with [26] in 2013, where the validity of the asymptotic formulas given in [25] in DIII-D and ITER were analyzed, and the importance of taking the full runaway electron distribution function into account was pointed out. In 2014, the theory derived in both [24] and [25] was applied to the EAST tokamak in [27], and analysis of the spot shape dependence on pitch angle and safety factor was done. Recently, more advanced synthetic synchrotron diagnostics have been developed that take both camera and magnetic field geometry into account. These are the *Kinetic Orbit Runaway electron Code* (KORC) [28, 29], which follows the runaway electron particle orbits and calculates the associated synchrotron radiation emission, and the *Synchrotron-detecting Orbit Following Toolkit* (SOFT) [30] which utilizes the guiding-center approximation to rapidly calculate the synchrotron radiation. In [30, 31], SOFT was applied to a specific Alcator C-Mod scenario in order to discern the effect of, among others, the runaway electron energy and radial density profile, and it was found that both are crucial for interpreting the synchrotron radiation spot.

Runaway electron bremsstrahlung is very similar to synchrotron radiation in that it too is directed almost entirely along the electron's velocity vector. Thus, much of the theory derived in [30] applies also to the study of bremsstrahlung and a synthetic diagnostic for runaway electron bremsstrahlung could hence be implemented similarly to synchrotron radiation in SOFT. In this paper, we have extended SOFT with bremsstrahlung capabilities and will use it to simulate the gamma ray imager (GRI) diagnostic [32, 33], situated at DIII-D. The GRI consists of a lead pinhole camera and an array of gamma-ray detectors and therefore provides both spatial and spectral resolution of runaway electron bremsstrahlung emission. The large amount of information provided by the GRI gives a unique view into the evolution of runaway electrons during experimental scenarios, and may be able to provide sufficient data for the first robust calculations of the runaway electron distribution function from runaway electron radiation measurements.

In this paper we investigate the leading causes behind the particular shape of a DIII-D synchrotron radiation image, and compare the distribution function predicted by a kinetic model for runaways to experimental synchrotron and bremsstrahlung measurements for the same experimental discharge. With a qualitative model and simulations we identify the sources of various features in the image and explain the characteristic crescent spot shape of the DIII-D synchrotron image. By solving the Fokker-Planck equation for runaways numerically we predict a distribution function for the runaways in the investigated DIII-D scenario in order to assess the validity of the model. We also present the first SOFT simulations of the GRI using which we discuss similarities and differences between observed runaway synchrotron and bremsstrahlung radiation.

In section 2, a qualitative model is presented and we identify the most important quantities affecting a synchrotron

radiation image to be the so called surface-of-visibility, the finite spectral range of the camera used and the distribution function. In section 3, kinetic simulations of the runaway electron distribution function in combination with SOFT simulations are conducted for DIII-D discharge 165826. The disagreement of these simulations with experiment is related to possibly missing physics in the kinetic model used. The paper concludes with a discussion in section 4 about what can be said about runaway electron radiation investigations in low-density scenarios similar to DIII-D discharge 165826.

2. Qualitative model of synchrotron radiation

Synchrotron radiation is emitted by highly relativistic charged particles in magnetic fields when they undergo circular motion [7, 8], and characteristic for this type of emission is the strong forward beaming of radiation along the particle's velocity vector. Because of this, electrons will only be visible to the observer in the regions of the tokamak where the electrons move directly towards the detector, and synchrotron radiation images therefore typically show synchrotron radiation 'spots' appearing on only one side of the tokamak. The angular spread of the emission is $\sim \gamma^{-1}$ (considering the average over all emitted wavelengths), where γ is the relativistic gamma factor, which for high energy runaway electrons means that the radiation can be approximated as emitted almost exactly on a straight line along the electron's velocity vector. The model in which this approximation is made, henceforth referred to as the 'cone model' for reasons soon to be explained, was implemented in the SOFT code [30] and compared to a model taking the full angular spread of the radiation into account. The comparison showed that these two models were in good agreement with each other. The simulations conducted in this paper will all use the cone model due to its superior computational performance.

The name of the cone model stems from the fact that the guiding-center of an electron can be seen as emitting a hollow cone of radiation with opening angle $\theta_p = \arccos(v_{\parallel}/v)$ around its velocity vector. It is assumed that all radiation is emitted uniformly across this cone, and in the cone model used in this paper it is further assumed that the synchrotron power received in a wavelength interval $[\lambda, \lambda + d\lambda]$ is given by [8]

$$\frac{dP}{d\lambda} = \frac{1}{\sqrt{3}} \frac{ce^2}{\epsilon_0 \lambda^3 \gamma^2} \int_{\lambda_c/\lambda}^{\infty} K_{5/3}(l) dl. \quad (1)$$

Here, c is the speed of light, e is the elementary charge, ϵ_0 is the permittivity of free space, γ is the Lorentz factor for the electron, $\lambda_c = 4\pi m_e c \gamma_{\parallel} / 3\gamma^2 e B$, m_e is the electron mass, $\gamma_{\parallel} = (1 - v_{\parallel}^2)^{-1/2}$, v_{\parallel} is the electron's speed along the magnetic field, B is the magnetic field strength and $K_{5/3}$ is a modified Bessel function of the second kind.

When analyzing synchrotron radiation from runaway electrons, it turns out that the appearance of synchrotron radiation spots as seen by a camera is determined mainly by three different effects:

- The so called surface-of-visibility (SOV), to be explained in section 2.1, which is a geometric feature and results from the anisotropy of the synchrotron radiation emission.
- The amount of radiation emitted and, more importantly, detected. The location of the wavelength interval that a synchrotron camera operates in can significantly alter the appearance of a synchrotron spot depending on how close it is to the peak wavelength of the radiation received by the camera.
- The momentum-space distribution function of runaway electrons, the shape of which determines which particles will dominate the emission.

In what follows we will describe the importance of each of these effects and show how a synchrotron spot can be built up successively by them.

2.1. Surface-of-visibility

Aside from bringing the computational advantages of not having to resolve the full gyro-orbit, the cone model also provides a simple framework for qualitative reasoning about the region from which synchrotron radiation can be detected. Since synchrotron radiation is only detected when the emitting particle is moving directly towards the detector, the overall shape of the observed synchrotron spot is mainly determined by the magnetic field geometry [24, 27]. Neglecting drift velocities, the cone model gives a very simple condition for a particle to be seen by the detector:

$$\left| \hat{\mathbf{b}}(\mathbf{x}) \cdot \hat{\mathbf{r}}(\mathbf{x}) \right| = |\cos \theta_p|. \quad (2)$$

Here $\hat{\mathbf{b}}(\mathbf{x})$ is the magnetic field unit vector in the point \mathbf{x} in space, $\hat{\mathbf{r}} = (\mathbf{x} - \mathbf{x}_0)/|\mathbf{x} - \mathbf{x}_0|$ is the unit vector pointing from the detector, located at \mathbf{x}_0 , to \mathbf{x} and θ_p is the pitch angle at \mathbf{x} under consideration. For a fixed value of θ_p , the solution to this equation is a surface in real space, which we call the *surface-of-visibility* (SOV). It is clear from equation (2) that aside from a strong dependence on the magnetic field and the particle's pitch angle, the shape of the SOV is also strongly dependent of the placement of the detector. None of the quantities involved in (2) however depends on the particle's energy, which means that the SOV is independent of the energy. In reality, drift orbits introduce an energy dependence, but these effects are neglected in the zeroth order guiding-center model we employ. In figure 1, different projections of the surface-of-visibility for a given \mathbf{x}_0 lying in the midplane and runaway-electron population with $\theta_p = 0.16$ rad and beam radius $r \approx 50$ cm in DIII-D is shown, revealing its cylindrical structure. Note that the surface-of-visibility in figure 1 is the surface corresponding to particles given an initial pitch angle $\theta_p = 0.16$ rad in the outer midplane. The pitch angle then varies together with the magnetic field along the particle orbit.

The importance of the magnetic field geometry for determining the synchrotron spot shape was emphasized already by Pankratov in 1996 [24], but the realization that what is perceived as a 'spot' in synchrotron images is in fact the

projection of a *surface* of finite toroidal extent could be even more important when considering momentum-space distributed populations of runaway electrons. The reason for this is that SOVs for particles with small pitch angles (typically $\theta_p \lesssim 0.20$ rad) close on themselves, and the line-integrated contribution from a line-of-sight passing through the edge of such a surface will be greater due to that the line-of-sight tangents the surface. The edges of the projected SOV therefore tend to be significantly brighter than other parts of the SOV, as is exemplified in figure 1. Because of this the edges of single-particle synchrotron spots (i.e. spots corresponding to a specific set of pitch angle θ_p and momentum p) tend to dominate synchrotron spots from momentum-space distributed runaway electron populations and 'fill in' different parts of the overall spot.

2.2. Synchrotron emission and camera spectral range

The amount of radiation emitted by a particle is another important quantity affecting the appearance of a synchrotron spot. Since the total synchrotron power emitted by an electron in a magnetic field is given by [7]

$$P = \frac{e^4}{6\pi\epsilon_0 m_e^2 c} p_\perp^2 B^2 \propto p_\perp^2 B^2 \propto p^2 B^3, \quad (3)$$

where p is momentum and $p_\perp = p \sin \theta_p \propto p\sqrt{B}$ is the component of p perpendicular to the magnetic field \mathbf{B} , we expect a particle to emit more radiation when it passes through the high-field side of a tokamak, both because the magnetic field is stronger there, and because of the larger pitch angle the particle will have due to the stronger magnetic field. It turns out however, that while the synchrotron emission from the high-field side is typically stronger than that from the low-field side, the amount of synchrotron radiation received by a camera from the high-field side can scale much more strongly with magnetic field than B^3 . In fact, as we will now show, the ratio between emission from the HFS to the emission from the LFS can be on the order of 10^6 in DIII-D.

The reason for the strong scaling of the detected radiation stems from the finite spectral range of the camera. In most present-day tokamaks, the runaway electrons emit most of their radiation at wavelengths around a few micrometers, while visible light cameras seeing wavelengths up to around 900 nm are used. In this case it can be shown that the short-wavelength ($\lambda \ll \lambda_c$) asymptotic expansion of equation (1) is [34]

$$\frac{dP}{d\lambda} \sim \exp\left(-\frac{\lambda_c}{\lambda}\right). \quad (4)$$

By introducing the critical radius

$$R_c = \frac{B_0 R_0}{2m_e} \left(\frac{3\gamma e \lambda \sqrt{\mu}}{\pi c^2} \right)^{2/3}, \quad (5)$$

with $\mu = p_\perp^2/2m_e B$ being the magnetic moment, and assuming the magnetic field strength as a function of major radius to be $B(R) = B_0 R_0/R$, where B_0 and R_0 are the magnetic field strength and major radial location respectively of the magnetic axis, we can write the detected synchrotron power as

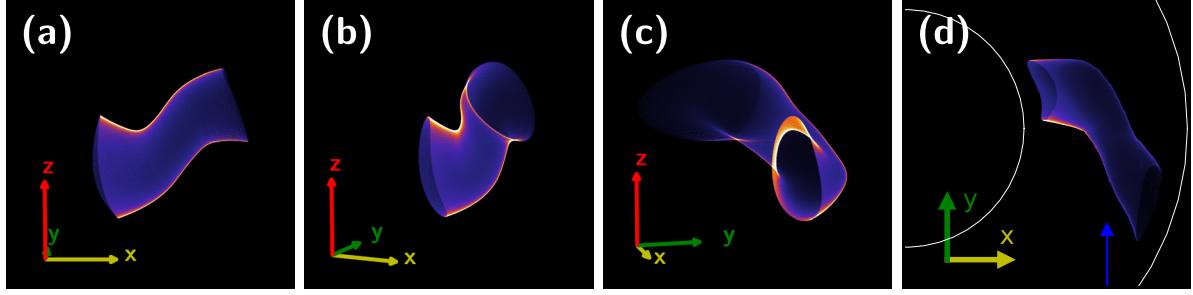


Figure 1. Different views of the surface-of-visibility corresponding to runaways with $\theta_p = 0.16$ rad in DIII-D. Between each of the figures (a)–(c) the SOV is rotated clockwise, and in (d) a top-down view of the tokamak and SOV is shown. The blue arrow in (d) indicates the location and direction of the camera.

$$P \sim \exp \left[- \left(\frac{R}{R_c} \right)^{3/2} \right]. \quad (6)$$

We can also express the ratio between maximum emission of a particle (at the innermost point of its orbit) to its minimum emission (at the outermost point of its orbit) as

$$\frac{P_{\max}}{P_{\min}} = \exp \left[\frac{(R_0 + \Delta R/2)^{3/2} - (R_0 - \Delta R/2)^{3/2}}{R_c^{3/2}} \right] \quad (7)$$

$$\approx \exp \left[\frac{3}{2} \frac{\Delta R}{R_0} \left(\frac{R_0}{R_c} \right)^{3/2} \right] \quad (8)$$

where ΔR is the distance between the inner- and outermost points of the particle orbit. The critical radius, $R_c = R_c(\lambda)$, can be interpreted as the major radius at which $\lambda_c = \lambda$, i.e. where the particle emits most of its radiation near the wavelength λ .

The exponential scaling with particle position equation (6) is the result of observing radiation in only a narrow range of wavelengths far from the wavelengths at which synchrotron emission peaks. In a typical DIII-D scenario, where $\lambda \approx 900$ nm and $\gamma \approx 30$, we find that $R_c \approx 0.1R_0$. A DIII-D runaway electron which moves a distance $\Delta R = 1$ m in major radius during its orbit therefore emits more on the high-field side compared to the low-field side by a factor $P_{\max}/P_{\min} \sim 10^6$, i.e. a six orders of magnitude difference. Had we instead been able to observe at a wavelength λ closer to λ_c , or even all radiation, the difference would merely have been about a factor of six. This shows that synchrotron radiation can appear significantly brighter in a region of space, without the number of runaways necessarily being higher in that region.

2.3. Runaway electron distribution function

In many previous studies, synchrotron spectra and spot shapes from single particles have been used to model experimentally observed spectra [11, 18] and spot shapes [27]. As was shown in [26] however, aside from the difficulties of interpreting the results (runaway electrons are rarely homogeneous enough for

a single particle to satisfactorily approximate the population), taking the distribution function of runaway electrons into account can significantly alter the simulated spectra. For the synchrotron spot, the difference can be even more dramatic, as the brightest features of a number of single particle-spot shapes will come together and create an overall pattern which does not necessarily resemble any of the single particle spot shapes.

The pitch angle and energy of a particle, together with the flux surface on which the particle moves (radial position), together determine the shape of the SOV and at which wavelength most of the synchrotron radiation is emitted. In figure 2 the effect of each of these parameters on the synchrotron spot is sketched and the arrows indicate how the spot shape changes with increasing pitch angle, energy and radial location. Figure 2(a) indicates that the pitch angle mainly determines the vertical extent of the SOV, while the radial location of the particle mainly affects the horizontal extent of the SOV, as shown in figure 2(c). The particle energy is mainly tied to the finite spectral range effect described in section 2.2, as is illustrated in figure 2(b). As the particle energy is increased, the peak of the emitted spectrum increases as well, meaning that the critical radius R_c also increases. For the synchrotron radiation spot this means that the low-field side part of the spot (right side of image) gains intensity relative to the high-field side part (left side of the image) giving a more even distribution of radiation horizontally across the SOV. A more in-depth description of how the spot shape varies with different parameters can be found in [30, 31].

The synchrotron spot of a certain population of runaway electrons will be the weighted average of several synchrotron spots, each corresponding to a unique set of runaway electron energy, pitch angle and radial location, i.e. individual particles. The weight is the distribution function which determines the relative importance of different particles in accordance with how likely they are to be found in the population and determines the overall spot shape.

A useful quantity that provides much information about the radiation from a distribution of runaway electrons is the density of radiation in momentum space,

$$F(p_{\parallel}, p_{\perp}) = \hat{I}(p_{\parallel}, p_{\perp}) f(p_{\parallel}, p_{\perp}), \quad (9)$$

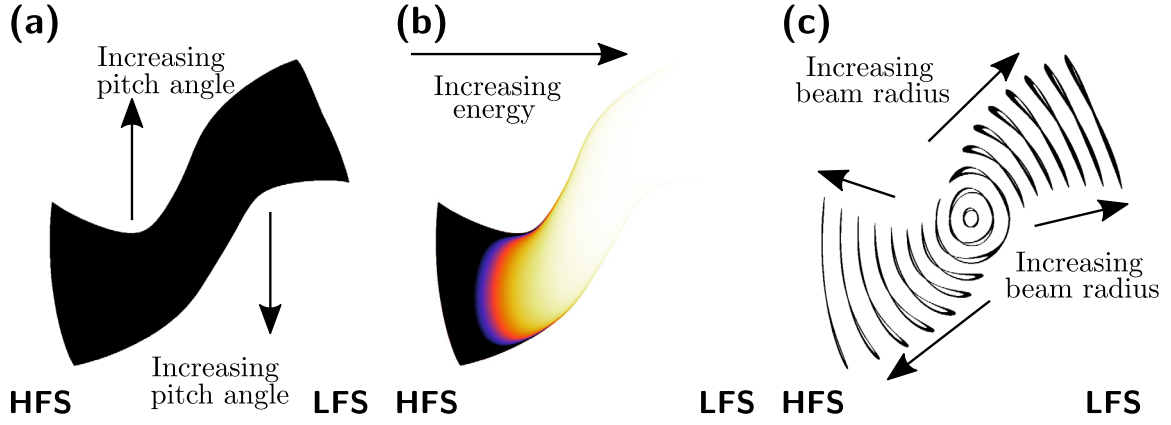


Figure 2. An illustration of how the three parameters of the runaway electron distribution function affect the shape of the synchrotron spot. The synchrotron radiation spot appears on the right side of the tokamak, i.e. to the right of the axis of symmetry. (a) A larger pitch angle implies greater vertical extent of the synchrotron spot and mainly affects the SOV. (b) Due to the finite spectral range effect of section 2.2, increasing the runaway electron energy causes radiation intensity to increase on the LFS relative to the HFS. (c) A larger runaway electron beam causes the synchrotron spot to be larger in the horizontal direction. Each of the slices of the spot in (c) comes from particles initiated at one radius, and they converge towards the magnetic axis in the center of the spot.

where $f(p_{\parallel}, p_{\perp})$ is the runaway electron distribution function and $\hat{I}(p_{\parallel}, p_{\perp})$ is the amount of radiation emitted by a particle with the given momentum, henceforth referred to as *weight function* (different for synchrotron or bremsstrahlung). Due to the p_{\perp}^2 scaling (or even stronger, as explained above) of the synchrotron emission, i.e. \hat{I}_s , the most numerous particle type is not necessarily the one that emits the most synchrotron radiation. While \hat{I} tends to grow monotonically with momentum p , and f tends to decrease with p_{\parallel} and p_{\perp} , the radiation density F generally has a global maximum in momentum space different from $p_{\parallel} = p_{\perp} = 0$. The maximum of F can be considered a ‘super’-particle which will dominate emission of a particular radiation type from a given distribution of runaway electrons. Often, the single particle spectrum that best matches the distribution averaged spectrum is that of the super particle, and the observed spot shape from the distribution has often many similarities to the spot shape of the super particle. It should be noted though that the only significance of the super particle is that it is the maximum of F . It is not (necessarily) the particle with the highest energy or pitch angle, and no general statement about the most common electron momentum can be made.

2.4. Similarities to runaway bremsstrahlung emission

Just like synchrotron radiation, bremsstrahlung is highly anisotropic and directed mainly in the particle’s direction of motion for highly relativistic particles. The average angular spread of bremsstrahlung is the same γ^{-1} as for synchrotron radiation, which means that bremsstrahlung also gives rise to a surface-of-visibility as discussed above, that is the same as that of synchrotron radiation. The cone model used in SOFT for synchrotron radiation can thus also be used for bremsstrahlung, but with the formula for received synchrotron radiation power replaced with the formula for the number of bremsstrahlung photons dN_{γ} emitted per unit photon energy dk (using the Born-approximation cross-section for a fully ionized plasma [35] summed over all ion species)

$$\begin{aligned} \frac{dN_{\gamma}}{dk} = & \frac{\alpha n_e Z_{\text{eff}} e^4 v p'}{(4\pi\epsilon_0 m_e c^2)^2 k p} \left\{ \frac{4}{3} - 2\gamma'\gamma \frac{p^2 + p'^2}{p^2 p^2} + \epsilon \frac{\gamma'}{p^3} + \epsilon' \frac{\gamma}{p'^3} - \frac{\epsilon\epsilon'}{p'p} + L \left[\frac{8\gamma'\gamma}{3p'p} \right. \right. \\ & \left. \left. + k^2 \frac{\gamma'^2 \gamma^2 + p'^2 p^2}{p'^3 p^3} + \frac{k}{2p'p} \left(\epsilon \frac{\gamma'\gamma + p^2}{p^3} - \epsilon' \frac{\gamma'\gamma + p'^2}{p'^3} + 2k \frac{\gamma'\gamma}{p'^2 p^2} \right) \right] \right\}, \\ \epsilon = & \ln \frac{\gamma + p}{\gamma - p} \\ \epsilon' = & \ln \frac{\gamma' + p'}{\gamma' - p'} \\ L = & 2 \ln \frac{\gamma'\gamma + p'p - 1}{k}, \end{aligned} \quad (10)$$

where $\alpha = e^2/4\pi\epsilon_0\hbar c \approx 1/137$ is the fine-structure constant, the photon energy k is defined in units of $m_e c^2$, and the normalized ingoing and outgoing electron momenta $p = \gamma v/c$ and p' are related through $p' = \sqrt{\gamma'^2 - 1}$, and $\gamma' = \gamma - k$.

Measurements of bremsstrahlung from runaway electrons is today a standard diagnostic at most larger tokamak experiments, and the data acquired is often used to study the temporal evolution of runaway electrons and sometimes even to measure the runaway electron energy distribution function [36, 37]. Bremsstrahlung from runaways has also previously been modeled, for example in the Tore Supra tokamak [38, 39]. At DIII-D, a novel technique for measuring not only the bremsstrahlung spectrum, but also its spatial distribution, has been developed and is called the GRI [32, 33]. The GRI combines a lead pinhole camera with gamma-ray detectors, thus functioning as a camera for gamma rays with energies in the range 1–60 MeV. From a theoretical point-of-view, the GRI is an ideal tool for studying runaways since the spectrum is also measured by each gamma-ray detector, thus providing a set of images at different photon-energies rather than just one single image. The weak pitch angle dependence in the bremsstrahlung emission is also advantageous, as it avoids the finite spectral range effect experienced with synchrotron radiation, which tends to obscure large parts of the spatial information.

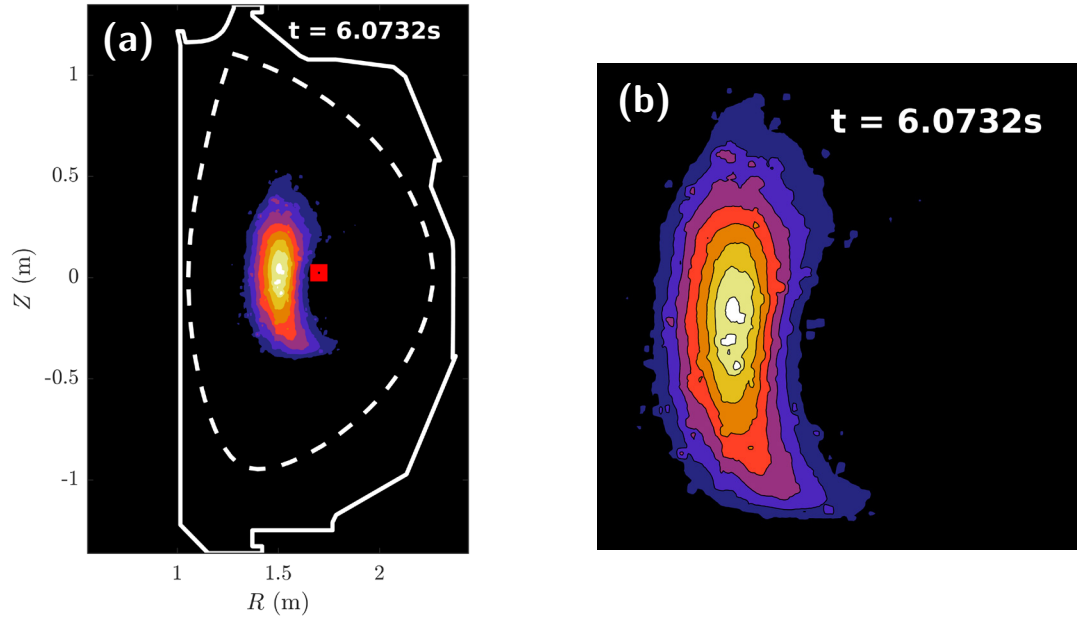


Figure 3. Synchrotron radiation from runaway electrons observed at $t = 6.0732$ s during DIII-D discharge 165826. (a) Synchrotron radiation mapped to the tangency plane with a wall cross-section and separatrix curve overlaid. The red marker indicates the location of the magnetic axis. (b) Synchrotron radiation in the pixel plane.

3. Runaway electron radiation images in DIII-D

Comparing and validating models of runaway electron dynamics against experiments is of crucial importance in order for any confidence to put in the models. The strong dependence on the distribution function seen in both synchrotron and bremsstrahlung emission, as discussed in the previous section, makes both types of radiation attractive diagnostics for this purpose. In this section we start by solving the spatially homogeneous kinetic equation numerically, taking plasma parameters from a DIII-D discharge as input, and use SOFT to compute the corresponding synchrotron and bremsstrahlung images. As the synthetic synchrotron images are found to disagree with the experimental images, we assess the properties required by the distribution function for agreement. We conclude the section with an analysis of bremsstrahlung images, which we compare to experimental data and discuss similarities and differences to synchrotron images.

We will analyze DIII-D discharge 165826 [36], a quiescent flat-top runaway discharge [20] which is carried out in two phases. In the first, low-density phase the runaway electron population is steadily built up through mainly primary (Dreicer) generation. When the runaway electrons have reached a critical density, nitrogen and deuterium is injected to initiate the dissipation phase, during which primary runaway electron generation ceases and effects such as avalanche generation and synchrotron/bremsstrahlung damping play a key role in the evolution of the runaway electron distribution function.

The fast synchrotron camera diagnostic used during the discharge was directed tangentially towards the plasma and detected all radiation emitted in a narrow band near wavelength 890 nm. It shows a characteristic crescent synchrotron

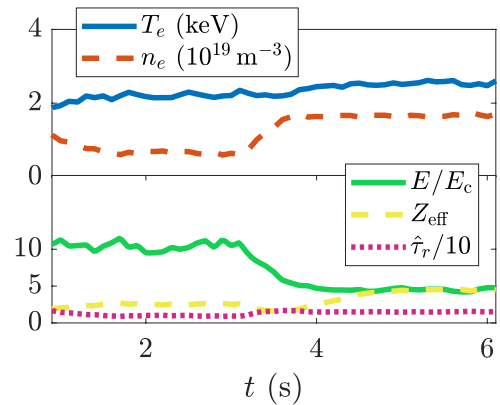


Figure 4. Temporal evolution during DIII-D discharge 165826 of the electron temperature T_e , electron density n_e (upper plot), toroidal electric field normalized to the critical electric field E_c , the effective charge of the plasma Z_{eff} and ratio of the collision to synchrotron damping time $\hat{\tau}_r$ (lower plot).

radiation spot shape, mainly originating from the HFS, with a maximum that is approximately vertically aligned with the magnetic axis, similar to what has been observed in other DIII-D low-density discharges [20].

For the following discussion we pick the synchrotron image corresponding to $t = 6.0732$ s, which is shown in figure 3 and is representative for the discharge. The image reveals that most of the synchrotron radiation is seen on the HFS, which based on our discussion in section 2.2 suggests that the dominating runaway electrons emit most of their radiation at a wavelength $\lambda_c \gg 890$ nm. The relatively large vertical extent of the radiation also suggests that the dominating particles have pitch angles above $\theta_p \sim 0.25$ rad, an estimate that is arrived at through simulation of single-particle synchrotron radiation images.

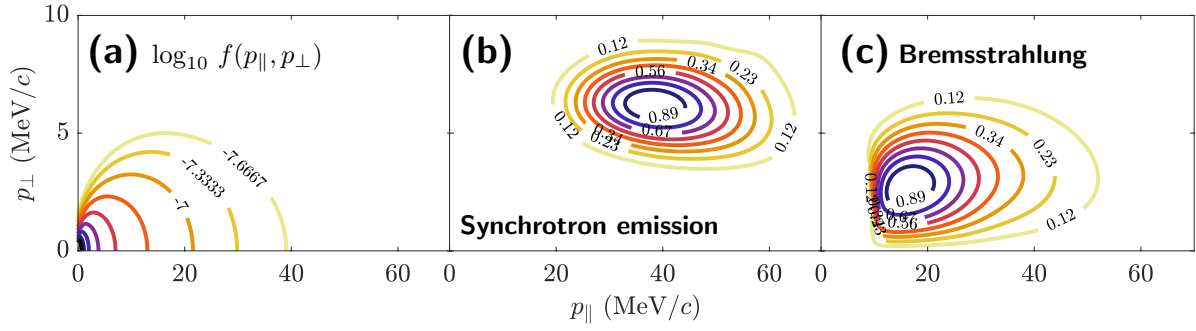


Figure 5. Plot of (a) the simulated distribution function described in section 3.1, (b) the synchrotron radiation emission in momentum-space from the distribution function F_s in the wavelength interval $\lambda \in [880, 900]$ nm and (c) the bremsstrahlung emission in momentum-space from the distribution function F_b at photon energy 9 MeV, with F_s and F_b defined in equation (9).

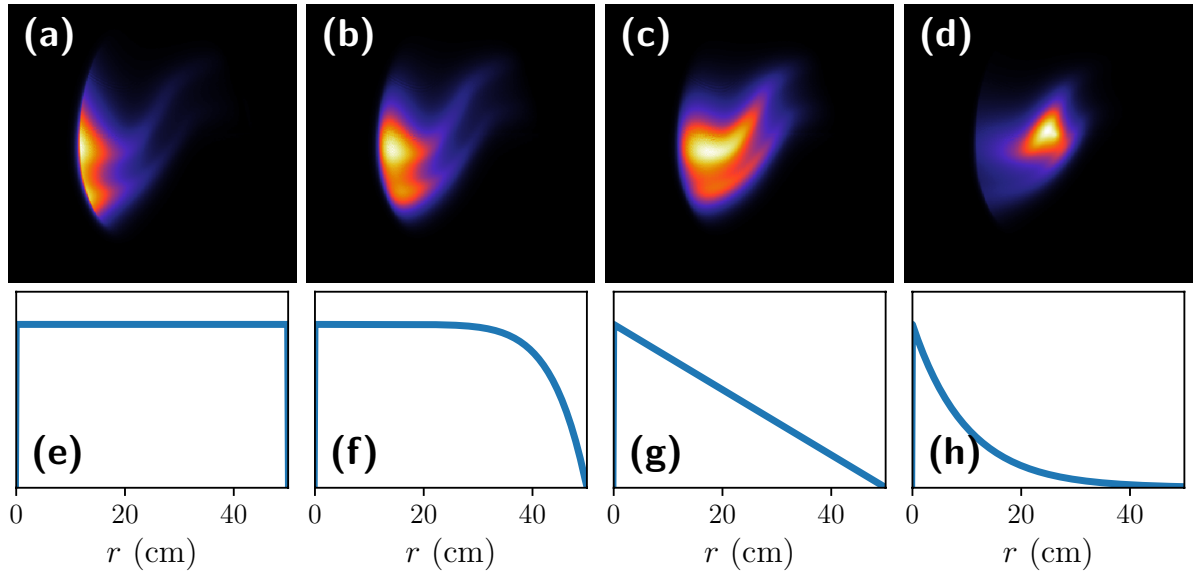


Figure 6. Synthetic synchrotron image resulting from the simulated distribution function figure 5(a). Four different radial density profiles have been applied to this image to discern the possible shape of the actual radial density profile. (a/e) Uniform/constant profile, cut off at $r = 50$ cm. (b/f) Eighth-degree polynomial. (c/g) Linearly decreasing profile. (d/h) Exponentially decreasing profile. All profiles are plotted against minor radius, so that $r = 0$ corresponds to the magnetic axis.

3.1. Kinetic modeling of the discharge

The temporal evolution of the 2D runaway electron momentum-space distribution function during DIII-D discharge 165826 was simulated using CODE [40, 41] by solving the spatially homogeneous kinetic equation, including electric-field acceleration, collisions modeled by a linearized Fokker–Planck operator, avalanche source and synchrotron-radiation reaction losses. Temporal profiles of electron temperature, density, toroidal electric field and plasma effective charge used in the calculation are shown in figure 4. All parameter profiles were measured at the magnetic axis, except for the electric field which was measured at the plasma edge. Because of this, the calculated momentum-space distribution function is formally only valid on the magnetic axis, but since the pitch-angles of most runaways in the resulting distribution are very small, so that trapping effects are negligible, we can use the same momentum-space distribution at all radii. We therefore take the obtained distribution function to be the distribution of runaways in the outer midplane. The electric field relaxation time is expected to be much shorter than the discharge time though,

so that the radial profile of the electric field is expected to be approximately uniform.

In figure 5, the resulting distribution function and corresponding synchrotron emission in momentum-space are shown. The relatively large number of runaway electrons with high energies causes the synchrotron emission to be dominated by runaway electrons with ~ 30 MeV energies and ~ 0.13 rad pitch angles. With bremsstrahlung we instead observe a different part of momentum-space, as the dominant runaways have energies around ~ 22 MeV and pitch-angles ~ 0.13 rad, as illustrated in figure 5(c).

3.2. Synchrotron radiation

The synthetic synchrotron image resulting from the distribution function in figure 5 is shown in figure 6 with four different radial density profiles applied to it, with the additional assumption that the momentum-space distribution is the same at all radii. As is seen in figure 6, the radiation originates mainly from the HFS, which should be due to the finite spectral range effect described in section 2.2. It is clear from figure 6

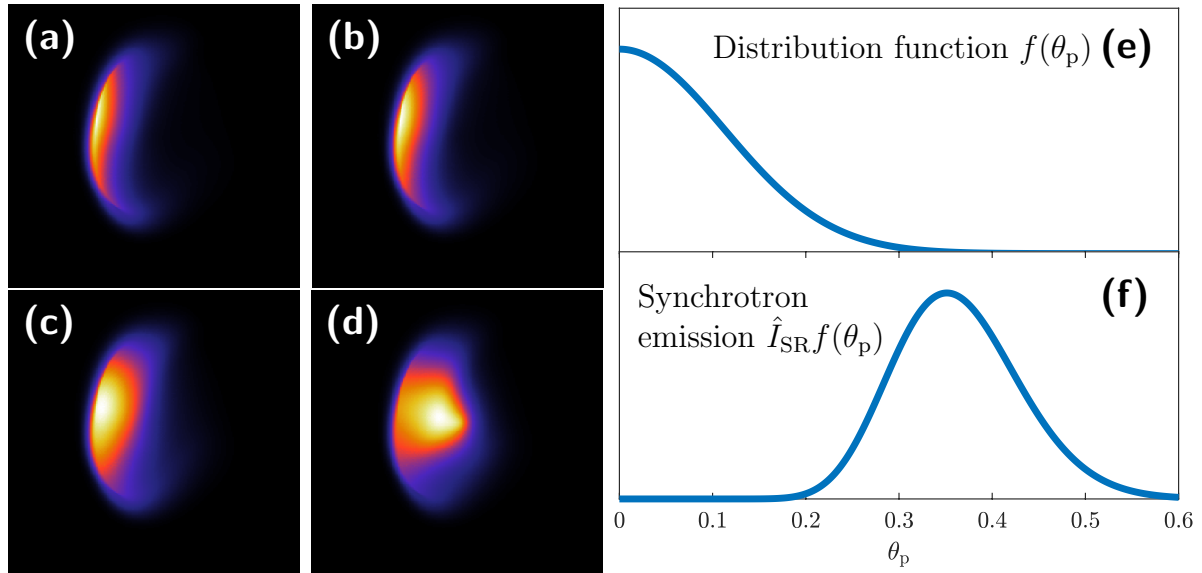


Figure 7. Synchrotron images resulting from simulations with the toy distribution function shown in (e) with one runaway electron energy, $E = 25$ MeV. In (a)–(d) the radial density profiles in figures 6(e)–(h) have been applied. Part (f) shows the distribution function weighed with the synchrotron emission in pitch angle-space, which reveals that the dominating particle should have a pitch angle $\theta_p \sim 0.35$ rad.

that none of the assumed radial density profiles is suitable to reproduce all the details of the experimental image. Due to the smooth decrease in intensity towards the HFS in the experimental image figure 3, the radial density profile should have to decrease smoothly to zero at larger radii, as in figures 6(b)–(d).

The rather wide spot obtained with a linearly decreasing profile, and the significant contribution from near the magnetic axis with the exponentially decreasing profile, suggests that such a rapidly decreasing profile is unlikely to explain the experimental image, at least with the momentum-space distribution used here. An off-axis peak in the radial density profile would provide even better agreement between simulation and experiment, however the two distinct, bright patches seen in the simulations would not go away with just a change in the radial distribution. Instead, the most plausible explanation is that the experimental runaway electron momentum-space distribution is different from the one predicted by solutions of the spatially homogeneous kinetic equation. There are important effects missing from this model, such as the effect of magnetic trapping, radial transport and drift-orbit losses that may be relevant to this DIII-D scenario. One further indication that it is the kinetic physics utilized that is not complete is, as mentioned, the appearance of two distinct, bright, vertically separated patches in the synthetic images. These bright patches should stem from the edges of the dominating SOV, and thus be the result of the line-integration effects described in section 1. The absence of these bright patches in experiment suggest that the experimentally observed SOV does not close on itself, which means that the dominating pitch angle must be much larger than the dominating pitch angle of the simulation.

The idea that kinetic processes not covered by the model employed are present in this DIII-D discharge was also suggested by [36], where radial transport or a kinetic instability was given as possible explanations. The evidence for this provided by [36] was an energy distribution function inverted from measurements with the GRI diagnostic, which did not match the distribution function

obtained from kinetic simulations. The inverted distribution function in [36] was characterized by much lower maximum energies than the corresponding simulated distribution function. This should make the difference between the high- and low-field side contributions more distinct in figure 6 and more consistent with figure 3.

To test the hypothesis that figure 3 is consistent with the dominating particle having a lower energy and larger pitch angle, a toy distribution function where all particles have the same energy $E = 25$ MeV but are distributed in pitch-angle so that the dominating particle has a pitch angle $\theta_p \sim 0.35$ rad. The distribution function is shown in figure 7(e), and in figure 7(f) the distribution function has been weighed with the synchrotron radiation weight function \hat{I}_s (see section 2.3) to reveal from where in pitch-angle space that most synchrotron radiation will be emitted. In figures 7(a)–(d) the resulting synthetic synchrotron image is shown, with the radial density profiles of figures 6(e)–(h) applied in order.

Of the synthetic images resulting from the toy distribution function in figure 7, it is figures 7(a) and (b) that most resemble the experimental image in figure 7. They all have a crescent shape with only one bright patch, and in both figures 3 and 7(a), (b) the bottom end of the spot extends slightly further to the LFS than the upper end. This provides further evidence for the conclusion that additional kinetic effects beyond those included in the spatially-homogeneous model need to be invoked in order to understand the measurements. An additional energy-limiting mechanism could shift the distribution to lower energies, where the higher rate of pitch-angle scattering could plausibly produce the required shape of the runaway distribution.

3.3. Bremsstrahlung

In figure 8, synthetic GRI images from mono-energetic and mono-pitch distributions simulated with SOFT are shown. Detectors are projected onto the poloidal plane orthogonal

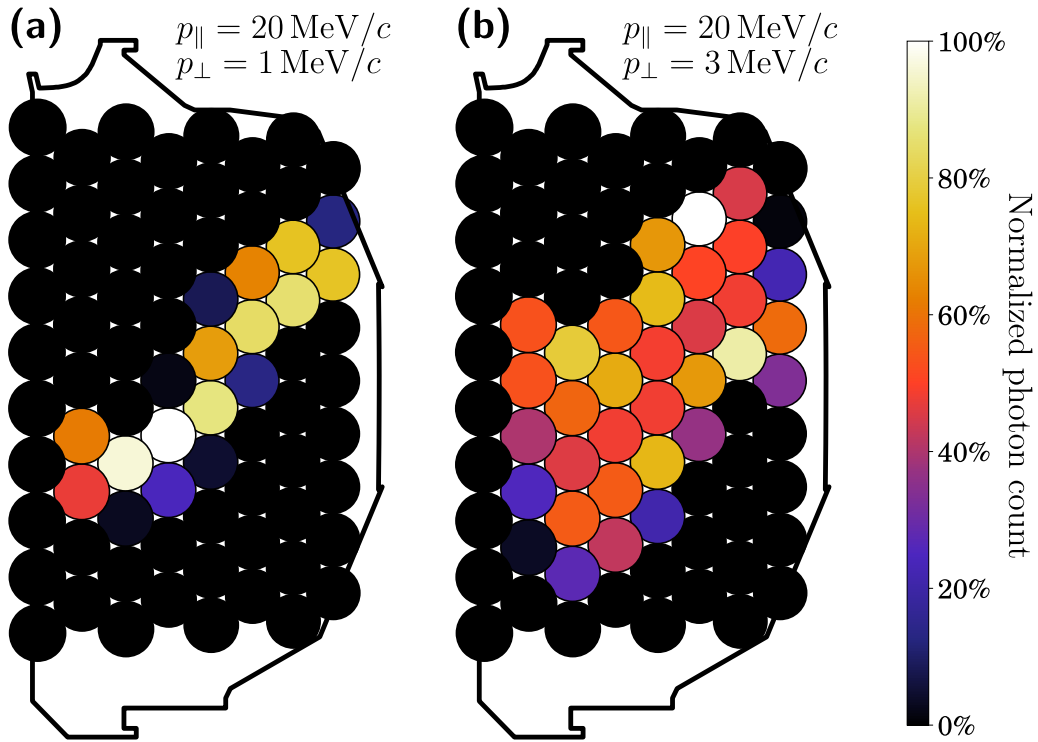


Figure 8. Synthetic GRI images resulting from particles with parallel momentum $p_{\parallel} = 20 \text{ MeV } c^{-1}$ and perpendicular momentum (a) $p_{\perp} = 1 \text{ MeV } c^{-1}$ and (b) $p_{\perp} = 3 \text{ MeV } c^{-1}$ respectively. The runaway electron beam radius was set to 50 cm and the detectors see photons in the range 1–60 MeV uniformly. The colors indicate photon counts, normalized to the maximum number of photon counts seen by any detector.

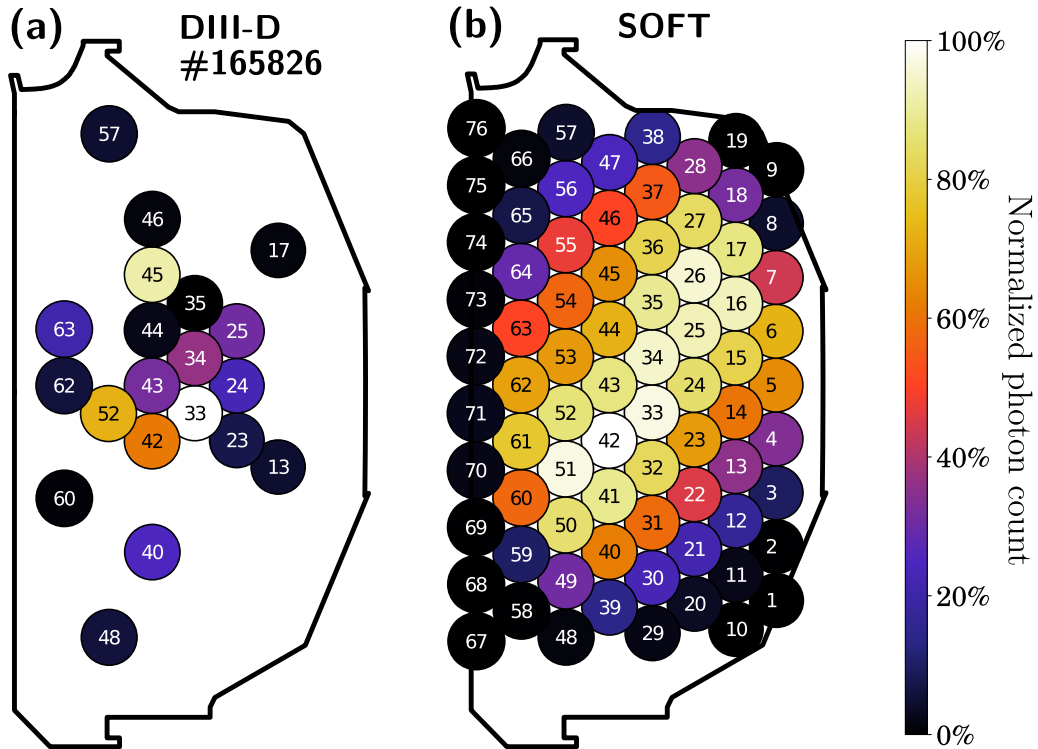


Figure 9. Comparison of (a) a GRI image reconstructed from experimental measurements to (b) a synthetic GRI image. The images show only radiation from the 9 MeV photon channel. All numbers correspond to detector indices. The colors indicate photon counts, normalized to the maximum number of photon counts seen by any detector.

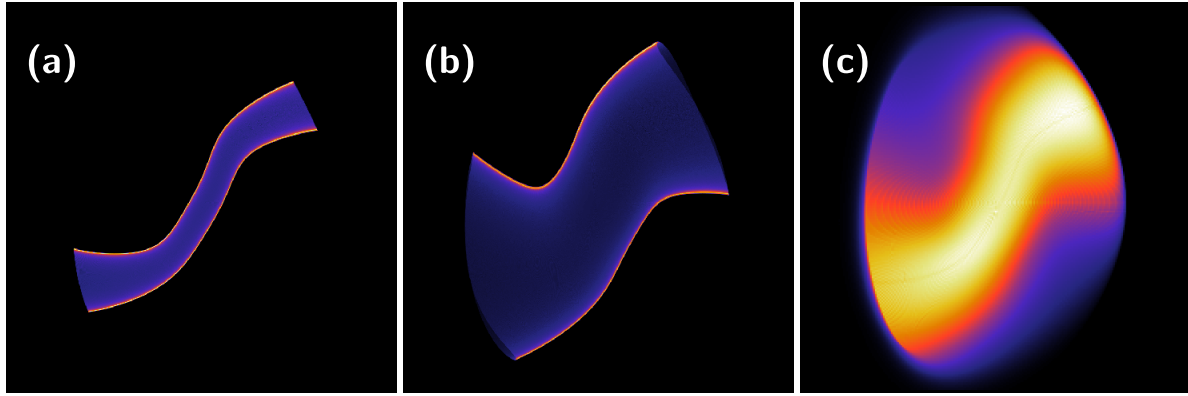


Figure 10. Bremsstrahlung images simulated with a synthetic high-resolution gamma-ray camera. Parts (a) and (b) result from single-particle simulations and correspond to the synthetic GRI images in figure 8, where $p_{\parallel} = 20 \text{ MeV } c^{-1}$ and (a) $p_{\perp} = 1 \text{ MeV } c^{-1}$ and (b) $p_{\perp} = 3 \text{ MeV } c^{-1}$. Part (c) results from a simulation with the distribution function in figure 5(a), and corresponds to the GRI image in figure 9.

to the viewing direction of a central detector (no. 43 in figure 9, not considering the z component of the viewing vector). In figure 8(a), a runaway electron beam with a 50 cm radius was initialized with parallel and perpendicular momentum $p_{\parallel} = 20 \text{ MeV } c^{-1}$ and $p_{\perp} = 1 \text{ MeV } c^{-1}$, while in figure 8(b) the particles were given $p_{\parallel} = 20 \text{ MeV } c^{-1}$ and $p_{\perp} = 3 \text{ MeV } c^{-1}$. The overall shape of the bremsstrahlung ‘spot’ is the characteristic projection of a twisted cylinder, which results from the same SOV as synchrotron radiation, and in contrast to what we see in the synchrotron radiation images, the amount of radiation coming from the HFS and LFS seem to be roughly the same, due to the lack of a pitch angle dependence in the emitted bremsstrahlung spectrum equation (10). The pitch angle does affect the spatial distribution of the bremsstrahlung though, since it determines the size and shape of the SOV. The effect of the runaway electron distribution function parameters on a bremsstrahlung image is therefore the same as shown for synchrotron radiation in figure 2, except for the camera finite spectral range effect in figure 2(b) which is completely absent.

The GRI was also used to determine the spatial distribution of bremsstrahlung during DIII-D discharge 165826, and the resulting measurement is shown in figure 9(a). In figure 9(b), the synthetic GRI image resulting from a SOFT simulation with the distribution function shown in figure 5(a) is displayed. Due to the few detector channels available in the measured GRI data, a quantitative comparison is not possible at this time and further analysis is left for the future when more detector channels are available.

The relation between the bremsstrahlung and synchrotron radiation images becomes more apparent by using a more idealized synthetic camera for the bremsstrahlung simulation, as done in figure 10. Both types of radiation give rise to exactly the same SOV, with the same bright edges, and the radial dependence must therefore also be the same. Bremsstrahlung, in contrast to synchrotron radiation, has a more uniform radiation intensity distribution across the SOV since it is independent of magnetic field-strength, which means that bremsstrahlung is seen roughly equally strongly on both the HFS and LFS. Based on figure 5(c), where the distribution function was weighed

with the bremsstrahlung emission, we expect a wide range of pitch angles to contribute significantly to the emission. In the image, this appears as a very bright, S-shaped band in the center of the image, with gradually decreasing intensity in both vertical directions. This is the behavior seen in the simulated GRI image in figure 9(b), and becomes even more apparent in the high-resolution bremsstrahlung camera image figure 10(c).

4. Conclusions

The synchrotron spot observed in runaway electron experiments is described in terms of the surface-of-visibility (SOV), the camera spectral range effect and the distribution function. The SOV determines the shape of the spot, while the camera spectral range determines the ratio of radiation seen on the HFS and LFS of the tokamak. The distribution function brings the individual synchrotron radiation spots from several classes of particles together and creates an overall spot shape, which combines the SOV and finite spectral range effect. Similar logic applies to bremsstrahlung, but due to the lack of pitch angle dependence in the bremsstrahlung emission, camera spectral range does not have the same dramatic effect on bremsstrahlung images, and its spatial localization depends only on the SOV.

An analysis of the formula for the synchrotron radiation spectrum in the limit of short wavelengths showed that the camera spectral range effect is very important in DIII-D, as the ratio between the intensity of synchrotron radiation on the HFS and LFS can be as high as 10^6 using a visible light camera. In a synchrotron image this causes the radiation from the HFS part of the image to completely dominate, and should in most cases appear as a crescent.

Based on the synchrotron radiation simulations conducted in section 3, we were able to conclude that the spatially homogeneous linear Fokker–Planck simulations of the runaway electron distribution function did not satisfactorily reproduce the synchrotron measurements. If the dominant particle however had lower energy and associated larger pitch angle, the pattern was more accurately reproduced. The same conclusion was reached in [36] for the same discharge and with a

similar kinetic model, but based on bremsstrahlung measurements, reinforcing the suspicion of the kinetic model being insufficient. Effects not considered by our kinetic model that could play an important role in this DIII-D scenario include magnetic trapping, radial transport and drift-orbit losses. To further test this hypothesis, a drift-kinetic solver that includes one spatial dimension such as LUKE [42–44] or CQL3D [45, 46] could be applied in order to also consider orbit effects.

Four different radial density profiles were applied to the simulated synchrotron images and compared to the experimental image. A smooth decrease to zero at the runaway electron beam edge is necessary to reproduce the observed synchrotron spot, and the best matching radial density profiles were those with a constant or almost constant behavior. There is great uncertainty about the shape of the radial density profile closer to the magnetic axis however, since the finite camera spectral range effect hides all but the radiation furthest out on the HFS, so that no data points are available there.

Simulations of the GRI were also conducted and compared to simulations of synchrotron radiation. While the spot shape seen with bremsstrahlung is still determined by the SOV, synchrotron and bremsstrahlung spots will generally look different and reveal different parts of momentum-space. The amount of information that could potentially be gained from GRI measurements in the future is however enormous, due to the availability of both spatial and spectral information from the diagnostic. The spatial information should be sufficient to constrain both the pitch angle and radial distribution functions, while the spectral data can be used to constrain the runaway electron energy. The independence on pitch angle and magnetic field strength of the bremsstrahlung emission also avoids the camera spectral range effect experienced with synchrotron radiation, which can conceal the distribution function near the magnetic axis. Thus the GRI is a promising diagnostic that, combined with simulations of the bremsstrahlung emission using SOFT, may be capable of finding more robust solutions to the inverse problem for the runaway electron distribution function.

Acknowledgments

The authors are grateful to L. Hesslow, O. Jakobsson, G. Papp, I. Pusztai, P. Svensson and G. Wilkie for fruitful discussions as well as the entire DIII-D team for excellent maintenance and operation of the tokamak. This work has been carried out within the framework of the EUROfusion Consortium and has received funding from the Euratom research and training programme 2014–2018 under grant agreement No 633053. The views and opinions expressed herein do not necessarily reflect those of the European Commission. The authors also acknowledge support from Vetenskapsrådet and the European Research Council (ERC-2014-CoG grant 647121). This material is based upon work supported by the U.S. Department of Energy, Office of Science, Office of Fusion Energy Sciences, using the DIII-D National Fusion Facility, a DOE Office of Science user facility, under Awards DE-FC02-04ER54698 and DE-FG02-07ER54917.

ORCID iDs

M. Hoppe  <https://orcid.org/0000-0003-3994-8977>
 C. Paz-Soldan  <https://orcid.org/0000-0001-5069-4934>
 R.A. Moyer  <https://orcid.org/0000-0002-3858-8159>
 T. Fülöp  <https://orcid.org/0000-0002-5898-0393>

References

- [1] Dreicer H. 1959 *Phys. Rev.* **115** 238
- [2] Jayakumar R., Fleischmann H.H. and Zweben S.J. 1993 *Phys. Lett. A* **172** 447
- [3] Rosenbluth M.N. and Putvinski S.V. 1997 *Nucl. Fusion* **37** 1355
- [4] Hollmann E.M. et al 2015 *Phys. Plasmas* **22** 021802
- [5] Hender T. et al 2007 *Nucl. Fusion* **47** S128
- [6] Boozer A.H. 2017 *Nucl. Fusion* **57** 056018
- [7] Schwinger J. 1949 *Phys. Rev.* **75** 1912
- [8] Bekefi G. 1966 *Radiation Processes in Plasmas* (New York: Wiley)
- [9] Finken K., Watkins J., Rusbüdt D., Corbett W., Dippel K., Goebel D. and Moyer R. 1990 *Nucl. Fusion* **30** 859
- [10] Jaspers R., Grewe T., Finken K., Krämer-Flecken A., Cardozo N.L., Mank G. and Waidmann G. 1995 *J. Nucl. Mater.* **220** 682
- [11] Jaspers R., Lopes Cardozo N.J., Donné A.J.H., Widdershoven H.L.M. and Finken K.H. 2001 *Rev. Sci. Instrum.* **72** 466
- [12] Wongrach K., Finken K., Abdullaev S., Koslowski R., Willi O., Zeng L. and (The TEXTOR Team) 2014 *Nucl. Fusion* **54** 043011
- [13] Esposito B., Martín-Solís J.R., Poli F.M., Mier J.A., Sánchez R. and Panaccione L. 2003 *Phys. Plasmas* **10** 2350
- [14] Esposito B. et al 2017 *Plasma Phys. Control. Fusion* **59** 014044
- [15] Tinguely R.A., Granetz R.S., Stahl A. and Mumgaard R. 2015 *57th Annual Meeting of the APS Division of Plasma Physics (Savannah, GA, 17 November 2015)*
- [16] Papp G. et al 2016 Runaway electron generation and mitigation on the european medium sized tokamaks ASDEX Upgrade and TCV *Preprint 2016 IAEA Fusion Energy Conf. (Kyoto, Japan, 17–22 October 2016)* eX/9-4 (<https://nucleus.iaea.org/sites/fusionportal/Shared%20Documents/FEC%202016/fec2016-preprints/preprint0502.pdf>)
- [17] Vlaine M., Mlynar J., Cavalier J., Weinzettl V., Paprok R., Imrisek M., Ficker O., Varavin M., Vondracek P. and Noterdaeme J.M. 2015 *J. Plasma Phys.* **81** 475810506
- [18] Yu J.H., Hollmann E.M., Commaux N., Eidietis N.W., Humphreys D.A., James A.N., Jernigan T.C. and Moyer R.A. 2013 *Phys. Plasmas* **20** 042113
- [19] Hollmann E. et al 2013 *Nucl. Fusion* **53** 083004
- [20] Paz-Soldan C. et al 2014 *Phys. Plasmas* **21** 022514
- [21] Zhou R.J. et al 2013 *Plasma Phys. Control. Fusion* **55** 055006
- [22] Cheon M., Kim J., An Y., Seo D. and Kim H. 2016 *Nucl. Fusion* **56** 126004
- [23] Tong R.H., Chen Z.Y., Zhang M., Huang D.W., Yan W. and Zhuang G. 2016 *Rev. Sci. Instrum.* **87** 11E113
- [24] Pankratov I.M. 1996 *Plasma Phys. Rep.* **22** 535
- [25] Pankratov I.M. 1999 *Plasma Phys. Rep.* **25** 145
- [26] Stahl A., Landreman M., Papp G., Hollmann E. and Fülöp T. 2013 *Phys. Plasmas* **20** 093302
- [27] Zhou R.J., Pankratov I.M., Hu L.Q., Xu M. and Yang J.H. 2014 *Phys. Plasmas* **21** 063302
- [28] Carbajal L., del Castillo-Negrete D., Spong D., Seal S. and Baylor L. 2017 *Phys. Plasmas* **24** 042512
- [29] Carbajal L. and del Castillo-Negrete D. 2017 *Plasma Phys. Control. Fusion* **59** 124001

- [30] Hoppe M., Embréus O., Tinguely R.A., Granetz R.S., Stahl A. and Fülöp T. 2018 *Nucl. Fusion* **58** 026032
- [31] Hoppe M. 2017 Synthetic synchrotron diagnostics for runaways in tokamaks *Master's Thesis* Chalmers University of Technology (<http://publications.lib.chalmers.se/records/fulltext/249436/249436.pdf>)
- [32] Pace D.C., Cooper C.M., Taussig D., Eidietis N.W., Hollmann E.M., Riso V., Van Zeeland M.A. and Watkins M. 2016 *Rev. Sci. Instrum.* **87** 043507
- [33] Cooper C.M., Pace D.C., Paz-Soldan C., Commaux N., Eidietis N.W., Hollmann E.M. and Shiraki D. 2016 *Rev. Sci. Instrum.* **87** 11E602
- [34] Jackson J.D. 1999 *Classical Electrodynamics* (New York: Wiley)
- [35] Koch H.W. and Motz J.W. 1959 *Rev. Mod. Phys.* **31** 920
- [36] Paz-Soldan C. et al 2017 *Phys. Rev. Lett.* **118** 255002
- [37] Shevelev A.E. et al 2017 *Nucl. Fusion* **58** 016034
- [38] Peysson Y. and Decker J. 2008 *Phys. Plasmas* **15** 092509
- [39] Nilsson E. et al 2012 Comparative modelling of LHCD with passive-active and fully-active multijunction launchers in the Tore Supra tokamak *39th EPS Conference on Plasma Physics (Stockholm, Sweden, 2–6 July 2012)* (<http://ocs.ciemat.es/EPSICPP2012PAP/pdf/P2.081.pdf>)
- [40] Landreman M., Stahl A. and Fülöp T. 2014 *Comput. Phys. Commun.* **185** 847
- [41] Stahl A., Embréus O., Papp G., Landreman M. and Fülöp T. 2016 *Nucl. Fusion* **56** 112009
- [42] Peysson Y., Decker J., Harvey R.W. and Forest C.B. 2003 Advanced 3D electron Fokker–Planck transport calculations *AIP Conf. Proc.* **694** 495
- [43] Decker J. and Peysson Y. 2004 DKE: A fast numerical solver for the 3D drift kinetic equation *Technical Report* EUR-CEA-FC-1736 Euratom-CEA
- [44] Nilsson E., Decker J., Peysson Y., Granetz R., Saint-Laurent F. and Vlainic M. 2015 *Plasma Phys. Control. Fusion* **57** 095006
- [45] Chiu S., Rosenbluth M., Harvey R. and Chan V. 1998 *Nucl. Fusion* **38** 1711
- [46] Harvey R., Chan V., Chiu S., Evans T., Rosenbluth M. and Whyte D. 2000 *Phys. Plasmas* **7** 4590–9